

ADVANCING ANALYTIC CLASS-INCREMENTAL LEARNING THROUGH VISION-LANGUAGE CALIBRATION

PREPRINT, COMPILED FEBRUARY 17, 2026

Bin Yu Zhao  ¹, Wei Zhang^{1,*}, Xingrui Yu  ^{2,*}, Zhaonian Zou  ¹, and Ivor Tsang  ²

¹School of Computer Science and Technology, Harbin Institute of Technology, China

²Centre for Frontier AI Research (CFAR), Agency for Science, Technology and Research (A*STAR), Singapore

ABSTRACT

Class-incremental learning (CIL) with pre-trained models (PTMs) faces a critical trade-off between efficient adaptation and long-term stability. While analytic learning enables rapid, recursive closed-form updates, its efficacy is often compromised by accumulated errors and feature incompatibility. In this paper, we first conduct a systematic study to dissect the failure modes of PTM-based analytic CIL, identifying representation rigidity as the primary bottleneck. Motivated by these insights, we propose **VILA**, a novel dual-branch framework that advances analytic CIL via a two-level vision-language calibration strategy. Specifically, we coherently fuse plastic, task-adapted features with a frozen, universal semantic anchor at the feature level through geometric calibration, and leverage cross-modal priors at the decision level to rectify prediction bias. This confluence maintains analytic-learning's extreme efficiency while overcoming its inherent brittleness. Extensive experiments across eight benchmarks demonstrate that VILA consistently yields superior performance, particularly in fine-grained and long-sequence scenarios. Our framework harmonizes high-fidelity prediction with the simplicity of analytic learning. Our code is available at <https://github.com/byzhaoAI/VILA>

1 INTRODUCTION

The capacity to acquire knowledge consecutively from non-stationary data streams is foundational for intelligent systems operating in dynamic real-world environments. Ideally, such systems must efficiently integrate new concepts while preserving previously mastered skills [1]. However, standard neural networks suffer from catastrophic forgetting when trained on shifting data distributions. While class-incremental learning (CIL) [2] aims to address this capability, achieving an optimal balance between stability (retaining old knowledge) and plasticity (learning new knowledge) remains a challenging objective.

Recent advancements have leveraged pre-trained models (PTMs) as a cornerstone strategy. PTMs provide robust, transferable feature representations that significantly elevate the performance baseline of CIL. However, the majority of PTM-based methods typically rely on iterative optimization of learnable parameters (e.g., via adapters or prompt tuning) [3, 4, 5, 6, 7, 8]. Although these methods have improved CIL performance, they are often prone to performance degradation as the number of tasks accumulates, driven by the progressive perturbation of the representation space by gradient updates. Moreover, some of them can be cumbersome to execute, requiring intricate training procedures and meticulous hyperparameter tuning to seek a delicate equilibrium between stability and plasticity, which hinders their deployment in efficiency-critical scenarios.

Analytic learning [9, 10] emerges as a compelling alternative path for CIL. By utilizing closed-form recursive least squares (RLS) updates, analytic learning transforms the learning process into a non-iterative matrix operation, offering mathematically optimal weights with theoretically zero forgetting of the learned mapping. Consequently, combining analytic learning with PTMs

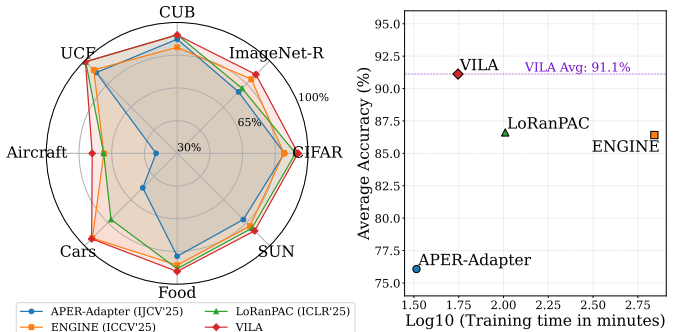


Figure 1: Performance and efficiency overview. (Left) Performance comparison across 8 diverse benchmarks. It demonstrates VILA's superior generality in both coarse- and fine-grained scenarios. (Right) Training time *vs.* Average accuracy. VILA occupies the optimal top-left corner, offering high-fidelity predictions with significantly lower latency.

presents a promising direction [11, 12, 13]. It aims to maintain high-level CIL performance by leveraging strong pre-trained features; Meanwhile, it alleviates the execution complexity and computational costs inherent to iterative methods.

Despite these advantages, we conduct a systematic analysis of this paradigm and identify a critical bottleneck termed *representation rigidity* that restricts its full potential. Our analysis suggests that while analytic learning effectively preserves historical knowledge within a given subspace, the feature space itself (typically frozen or narrowly adapted) may become rank-deficient for future distinct distributions. This implies that although analytic learning mitigates forgetting at the classifier level, it may lack the necessary feature plasticity to fully accommodate novel

*weizhang@hit.edu.cn, yu_xingrui@a-star.edu.sg

semantic clusters, potentially leading to accumulated approximation errors in long-term learning.

Based on this insight, we design **V**ision-**L**anguage **A**alytic learning (**VILA**), an asymmetric dual-branch framework to address the rigidity issue. VILA employs a two-level calibration strategy to seamlessly integrate the discriminative plasticity of a task-adapted Vision Transformer (ViT) with the generalizable stability of a frozen vision-language model (VLM). At the feature level, it geometrically aligns heterogeneous features onto a unified manifold. At the decision level, it utilizes semantic priors to rectify decision boundaries. Through this dual calibration, VILA effectively constructs a robust semantic subspace compatible with recursive updates. As shown in Figure 1, VILA demonstrates leading performance across 8 benchmarks, consistently outperforming iterative baselines with significantly higher training efficiency. The main contributions of this work are summarized as follows:

- We provide a systematic analysis of PTM-based analytic CIL. Our investigation exposes representation rigidity as a key bottleneck, and highlights the generalization constraints of single-branch architectures.
- We propose VILA, which integrates analytic learning with a frozen VLM via geometric and semantic calibration, effectively spanning a robust subspace to support continuous analytic updates.
- Extensive experiments demonstrate that VILA achieves superior performance and efficiency, offering a practical and robust solution for online class-incremental learning.

2 RELATED WORKS

Class-incremental learning (CIL). CIL is designed to continuously accumulate new knowledge from sequential data streams without erasing previously acquired capabilities. Traditional approaches generally fall into three paradigms. *Regularization-based* methods [14, 15] impose constraints on weight updates to preserve important parameters of prior tasks. *Replay-based* strategies [16, 17] maintain a memory buffer of historical exemplars to rehearse previous knowledge. *Architecture-based* approaches [18, 19] dynamically expand the network capacity to isolate task-specific parameters. While foundational, these methods often struggle to balance scalability and performance in large-scale settings.

PTM-based CIL. Traditional CIL methodologies were predominantly centered on training models from scratch. In contrast, recent advances have shifted this paradigm towards adapting PTMs. The dominant strategy is parameter-efficient fine-tuning (PEFT), which includes three parallel streams: *Prompt-based* methods [3, 4] that insert learnable tokens to instruct attention; *Adapter-based* methods [20, 21, 13] that inject bottleneck layers for feature modulation; and *LoRA-based* strategies [22, 5, 23, 24] that optimize low-rank updates. Despite their effectiveness, these iterative methods incur significant latency due to back-propagation.

Furthermore, VLMs have introduced a new dimension by leveraging large-scale image-text pre-training to align visual features

with rich linguistic semantics. This paradigm shifts the focus from closed-set classification to open-world recognition. While VLMs like CLIP [25] possess strong zero-shot classification capabilities, they often lack domain specialization and struggle with fine-grained distinctions (e.g., specific aircraft variants or medical conditions). To address this, recent VLM-based works [26, 27, 7, 28] aim to adapt these models to continuous streams. However, they typically rely on heavy tuning, or fail to fully exploit the geometric complementarity between visual adaptation and frozen semantic priors.

Analytic CIL. Distinct from gradient-based optimization, analytic learning converts training into a regularized least-squares problem, yielding closed-form solutions via recursive updates. Recent advances [11, 12] successfully scale this paradigm to PTMs by projecting high-quality deep features into a high-dimensional buffer. This approach offers theoretically guaranteed stability and extreme efficiency. However, the limitation of representation rigidity still remains. Since the analytic solver requires a fixed input distribution, existing methods are confined to frozen feature extractors, lacking the plasticity to accommodate semantic drift in long sequences. Our work bridges this gap by calibrating the analytic process with a dual-branch VLM framework.

3 PRELIMINARIES AND MOTIVATION

We consider the CIL setting where a model learns from a sequence of tasks $\mathcal{T} = \{1, \dots, T\}$. Each task t introduces a dataset $\mathcal{D}_t = \{(x_i, y_i)\}_{i=1}^{N_t}$ with inputs $x_i \in \mathcal{X}$ and labels $y_i \in \mathcal{C}_t$, satisfying $\mathcal{C}_{t_i} \cap \mathcal{C}_{t_j} = \emptyset$ for $i \neq j$. The objective is to optimize a composite function $f_\theta \circ W$, where f_θ is the feature extractor and W is the classifier, to minimize the prediction error on the union of all seen classes $\mathcal{C}_{0:t}$, strictly prohibiting access to raw data from previous tasks $\mathcal{T}_{<t}$.

3.1 Analytic CIL protocol

Analytic learning offers a recursive, closed-form alternative to gradient-based optimization. Following the ACIL protocol [29], the feature extractor f_θ is typically optimized *only on the first task* \mathcal{D}_1 and subsequently frozen to maintain a stationary feature distribution. To enhance linear separability, a fixed random projection buffer maps backbone features $\mathbf{F} = f_\theta(x) \in \mathbb{R}^D$ to a high-dimensional space $\mathbf{F}^B = \sigma(\mathbf{F}W^B) \in \mathbb{R}^{D_B}$, where W^B is a frozen Gaussian matrix and σ is the ReLU activation.

The learning objective at task t is to solve the ridge regression [30] problem for the classifier W :

$$\min_W \|\mathbf{F}^B W - Y^{OH}\|_F^2 + \lambda \|W\|_F^2 \quad (1)$$

where Y^{OH} denotes the one-hot label matrix. The optimal solution is given by $W = (\Phi + \lambda I)^{-1}(\mathbf{F}^B)^T Y^{OH}$, where $\Phi = (\mathbf{F}^B)^T \mathbf{F}^B$ is the autocorrelation matrix.

In the incremental setting, recursive least squares (RLS) is employed to update the inverse correlation matrix $R_t = (\Phi_t + \lambda I)^{-1}$ and classifier W_t derived from task $t-1$:

$$\begin{aligned} R_t &= R_{t-1} - R_{t-1}(\mathbf{F}_t^B)^T (I + \mathbf{F}_t^B R_{t-1}(\mathbf{F}_t^B)^T)^{-1} \mathbf{F}_t^B R_{t-1} \\ W_t &= W_{t-1} + R_t(\mathbf{F}_t^B)^T (Y_t^{OH} - \mathbf{F}_t^B W_{t-1}) \end{aligned} \quad (2)$$

Table 1: Pilot study on *representation rigidity*. Performance comparison (last-task accuracy A_T / average accuracy \bar{A}) of PTM-based analytic CIL. All fine-tuning (FT) modules are trained solely on the first task (\mathcal{D}_1) and subsequently frozen. "Visual Init" denotes initializing the backbone with CLIP's visual encoder weights without the text branch. The dimension of the random buffer is set to 8192.

Item	Configuration (PW + FT)	CIFAR (10 tasks)	CIFAR (20 tasks)	ImageNet-R (10 tasks)	ImageNet-R (20 tasks)
i	ViT (ViT-B/16, Fixed)	84.61/89.69	84.64/89.78	70.12/75.57	69.95/75.98
ii	ViT-PT (ViT-B/16 + Prompt Tuning)	71.25/80.34	48.12/59.70	68.63/75.10	70.93/76.86
iii	ViT-LoRA (ViT-B/16 + LoRA)	90.62/94.26	3.36/19.80	78.90/84.60	77.27/82.86
iv	ViT-Adapter (ViT-B/16 + Adapters)	90.80/94.33	89.39/93.43	77.78/82.94	76.17/81.79
v	CLIP-LoRA (CLIP-ViT (Visual Init) + LoRA)	68.90/78.98	49.18/62.72	25.48/35.98	12.68/21.11
vi	CLIP-Adapter (CLIP-ViT (Visual Init) + Adapters)	37.97/49.21	31.11/43.46	9.32/15.92	8.83/15.67

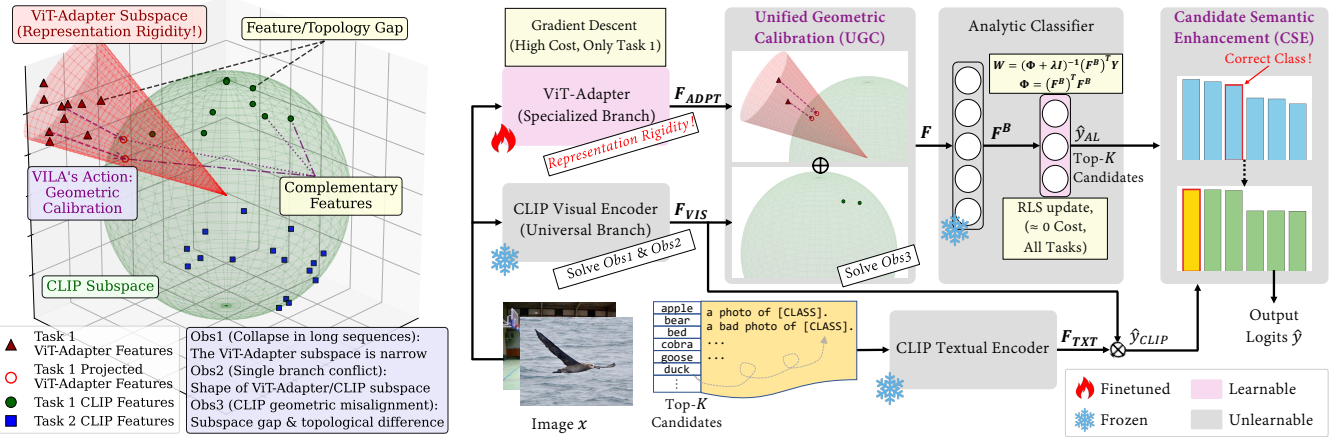


Figure 2: From observation to solution. **Left:** feature space trilemma. The specialized **ViT-Adapter** branch collapses into a rigid subspace, which creates a geometric misalignment with the universal **CLIP** hypersphere and fails to cover **future-task features**. **Right:** VILA asymmetric dual-branch architecture. It integrates a frozen universal branch to mitigate stability-plasticity dilemma (*Obs1 & Obs2*). The UGC module projects heterogeneous features onto a unified manifold to address misalignment (*Obs3*). The CSE module leverages text priors to rectify decision boundaries. Solely training on Task 1 and updating classifier via analytic learning ensures extreme efficiency.

The recursive dilemma. The validity of Eq. (2) strictly hinges on the stationarity of f_θ . The matrix R_{t-1} encapsulates the precise geometric structure of past data projected by $f_{\theta_{old}}$. Any update to θ (e.g., fine-tuning on Task t) would alter the mapping of past data, rendering the stored R_{t-1} invalid. We term this phenomenon *Gram Matrix Inconsistency*. This creates a dilemma: keeping f_θ frozen ensures stability but limits plasticity, while updating f_θ enables plasticity but destroys the recursive history.

3.2 Theoretical motivation: generalization gap in rigid representations

Under the standard protocol where θ is frozen after Task 1, performance degradation stems strictly from *representation rigidity*. We formalize this as a subspace approximation problem. Let the optimal semantic features for task t lie in a subspace \mathcal{V}_t . The feature extractor trained on Task 1 spans a fixed subspace $\mathcal{S}_1 = \text{span}(f_{\theta_1})$. The error on a future task t is lower-bounded by the projection residual of the task's ideal semantics onto the frozen feature space \mathcal{S}_1 .

Proposition 3.1 (Representation Rigidity Bound). Let $y \in \mathcal{Y}_t$ be the target function for a future task t . The expected approximation error of the analytic classifier is lower-bounded by the

alignment gap between the Task 1 distribution \mathcal{P}_1 and Task t distribution \mathcal{P}_t :

$$\mathcal{E}_{task_t} \geq \|(I - \mathbf{P}_{\mathcal{S}_1})y\|^2 \propto \text{Dist}(\mathcal{P}_1, \mathcal{P}_t) \quad (3)$$

where $\mathbf{P}_{\mathcal{S}_1}$ is the orthogonal projection operator onto the feature space learned on Task 1. (See Appendix A for derivation.)

This aligns with findings in transfer learning [31, 32], suggesting that fine-tuning on \mathcal{P}_1 aggressively rotates the feature manifold \mathcal{S}_1 to minimize empirical risk on Task 1. This specialization often renders the learned features effectively *orthogonal* to the semantic directions required for novel classes [32]. Consequently, the representation space suffers from a "semantic blind spot", where the specialized basis vectors fail to span the necessary variance for future distributions, creating a theoretical imperative for incorporating a complementary, invariant subspace.

3.3 Empirical verification: the plasticity-stability-geometry trilemma

To rigorously verify the theoretical bound derived in **Proposition 3.1**, we conducted an extensive series of pilot studies. For clarity and focus, we curate and present the most representative results in Table 1.

Obs1: Specialization on the initial task may lead to feature collapse in long sequences. Consistent with our rigidity bound, *ViT-LoRA* (iii) exhibit a stark contrast. While achieving superior accuracy on short sequences (90.62% on CIFAR 10 tasks), performance collapses on longer sequences (3.36% at 20 tasks). This confirms that optimizing exclusively for \mathcal{D}_1 may collapse the feature rank, rendering the specialized subspace \mathcal{S}_1 incapable of spanning the semantic dimensions for distant future tasks. This is visualized by the collapsed red distribution in Figure 2 (Left).

Obs2: A single branch cannot simultaneously satisfy the stability-plasticity dilemma. Comparing *ViT* (i) and *ViT-LoRA* (iii) reveals a fundamental conflict. The former maintains stability via its universal basis but lacks discriminability, while the latter gains initial plasticity but sacrifices OOD generalization. This validates that a single branch cannot simultaneously minimize the projection residual for both current and future tasks. Figure 2 (Left) shows a conflict illustrated by the topological divergence.

Obs3: Naive initialization with CLIP weights fails due to intrinsic geometric misalignment. Crucially, simply initializing the backbone with CLIP’s visual weights (v, vi) fails catastrophically in the analytic setting (e.g., 12.68% on ImageNet-R). This holds true regardless of standard preprocessing (ℓ_2 -normalization). We attribute this to *intrinsic geometric misalignment*: CLIP’s features are optimized for contrastive matching on a specific manifold, which is structurally incompatible with the RLS solver’s assumption of Euclidean linear separability (Eq. 1). As shown in Figure 2 (Left), neither direct projection nor simple normalization suffices to bridge the gap and construct a valid decision boundary.

The theoretical analysis and empirical evidence converge on a single conclusion: to break the representation rigidity bottleneck, we must design a system that (1) retains the *discriminative plasticity* of a specialized adapter, (2) anchors it with the *generalizable stability* of a universal baseline, and (3) *geometrically aligns* these heterogeneous subspaces. This motivates our VILA framework.

4 THE VILA FRAMEWORK: BRIDGING SPECIALIZED AND UNIVERSAL SUBSPACES

Motivated by the geometric bottlenecks identified above, we propose VILA, an asymmetric dual-branch framework designed to physically construct an ideal hypothesis space $\mathcal{S}_{total} = \mathcal{S}_{spec} \oplus \mathcal{S}_{uni}$. Here, \mathcal{S}_{spec} represents the specialized subspace that minimizes bias on the current task distribution, while \mathcal{S}_{uni} denotes the universal invariant subspace that bounds the projection residual for future tasks. The overall workflow is illustrated in Figure 2 (Right).

4.1 Asymmetric dual-branch architecture

The efficacy of VILA hinges on selecting the optimal backbone configurations to instantiate these two theoretical subspaces. We ground our architectural choices directly in the performance regimes observed in our pilot study (Sec 3.3).

Adapter-based specialized branch. We require a plastic component to capture the nuances of the initial task \mathcal{D}_1 . While various PEFT methods are candidates, our pilot study reveals a critical performance divergence. Despite its popularity, *ViT-LoRA* (iii) exhibits severe feature collapse on long sequences (CIFAR 20 tasks). We hypothesize that the strict low-rank constraint limits its adaptation capacity, resulting in underfitting on \mathcal{D}_1 . This failure yields a subspace that is inadequate for both current and future tasks. In contrast, *ViT-Adapter* (iv) maintain remarkable stability (89.39% at 20 tasks). This suggests that the bottleneck architecture better preserves the backbone’s pre-trained topology while offering sufficient plasticity. Consequently, we select the *ViT-Adapter* (f_{ADPT}) as our specialized branch, trained on \mathcal{D}_1 and subsequently frozen.

CLIP-based universal branch. To mitigate the “semantic blind spots” (null space) of the specialized branch, a secondary branch is required. However, training another ViT on the same data risks representational homogenization, converging to the same collapsed subspace. Therefore, we strategically employ a frozen CLIP as the universal anchor. Crucially, as shown in Table 1 (v, vi), CLIP features alone perform poorly in analytic classification. This indicates that while CLIP provides a rich “universal basis”, its features are not geometrically aligned for direct linear readout by the RLS solver. This observation necessitates the specific integration modules proposed below.

4.2 Unified geometric calibration (UGC)

Our first objective is to coherently merge the two branches into a unified feature vector \mathbf{F} . However, a direct concatenation faces a critical geometric misalignment. As analyzed in *Obs3* (Sec 3.3), CLIP features intrinsically reside on a hypersphere optimized for cosine similarity. In contrast, the supervised ViT-Adapter features occupy a high-magnitude unbounded Euclidean space.

To harmonize these heterogeneous representations, we introduce the unified geometric calibration (UGC). Given an input image x , we extract the universal features $\mathbf{F}_{VIS} = f_{CLIP}^{vis}(x) \in \mathbb{R}^{D_c}$ and the specialized features $\mathbf{F}_{ADPT} = f_{ADPT}(x) \in \mathbb{R}^D$. UGC projects the unbounded Adapter features onto the same hyperspherical manifold as CLIP via ℓ_2 -normalization. This calibration is essential to prevent the high-magnitude supervised features from numerically dominating the RLS update (Eq. 2), which would otherwise marginalize the contribution of the universal branch. The fused representation \mathbf{F} is defined as:

$$\mathbf{F} = \left[\frac{\mathbf{F}_{ADPT}}{\|\mathbf{F}_{ADPT}\|_2} ; \frac{\mathbf{F}_{VIS}}{\|\mathbf{F}_{VIS}\|_2} \right] \in \mathbb{R}^{D+D_c} \quad (4)$$

This calibrated concatenation physically realizes the direct sum $\mathcal{S}_{spec} \oplus \mathcal{S}_{uni}$. The aligned features are then projected via the random buffer W^B to $\mathbf{F}^B = \sigma(\mathbf{F}W^B)$, serving as the robust input for the analytic classifier.

4.3 Candidate semantic enhancement (CSE)

While the analytic classifier produces a robust primary prediction $\hat{y}_{AL} = \mathbf{F}^B W$, it fundamentally operates on a linear decision boundary within the random projection space. As the task sequence elongates, complex inter-class relationships (e.g., fine-grained species) may become linearly inseparable. To address this, we introduce a decision-level refinement that leverages the

Table 2: Comparison of last-task accuracy A_T (%) and average incremental accuracy \bar{A} (%) among PTM-based methods across diverse benchmarks. T denotes the total number of tasks. The best and second-best results are highlighted in **bold** and **blue**, respectively.

Metric	Dataset $T =$	CIFAR		ImageNet-R		CUB	UCF	Aircraft		Cars	Food	SUN		Avg.
		10	20	20	40	20	20	10	20	20	20	30	50	
A_T	L2P	84.29	77.70	70.13	65.07	64.21	72.41	28.74	18.90	20.52	70.03	57.41	54.98	57.03
	DualPrompt	82.30	77.23	65.98	60.13	65.95	76.17	25.50	10.14	18.66	69.22	62.23	62.03	56.29
	CODA-Prompt	86.85	79.59	70.33	61.02	68.45	76.09	27.24	15.54	15.31	72.32	64.88	58.49	58.01
	EASE	87.21	84.21	75.80	71.92	78.41	81.58	24.66	27.99	40.95	75.07	71.44	70.49	65.81
	APER-Adapter	85.80	82.77	70.52	66.70	84.68	86.66	30.96	30.93	41.69	77.98	72.51	72.46	66.97
	SD-LoRA	87.50	82.28	71.20	63.27	70.46	73.29	40.29	23.76	35.49	42.91	54.06	39.21	56.98
	CL-LoRA	88.17	84.91	78.40	73.50	73.92	79.23	45.57	26.76	40.46	76.42	71.34	69.27	67.33
	ENGINE	79.29	79.10	80.47	80.03	78.54	87.91	58.69	55.51	89.49	83.88	78.16	77.99	77.42
	RanPAC	86.40	86.36	71.83	71.70	88.93	97.73	59.23	58.33	66.81	84.56	79.65	79.75	77.61
	LoRanPAC	91.32	90.34	74.95	73.42	90.25	98.22	59.38	59.32	70.17	86.84	80.77	80.76	79.64
\bar{A}	VILA (Ours)	91.94	91.18	85.28	84.20	89.36	98.71	68.02	65.56	90.28	88.89	83.73	83.55	85.06
	L2P	89.23	84.20	75.86	72.04	75.93	83.58	41.79	32.32	29.92	77.62	68.54	66.45	66.46
	DualPrompt	87.36	84.85	72.53	68.23	76.44	86.05	40.12	23.57	31.05	79.58	73.64	73.17	66.38
	CODA-Prompt	91.30	86.17	75.93	66.48	76.57	84.87	30.50	19.44	33.08	81.39	76.95	72.07	66.23
	EASE	92.04	90.62	81.92	78.81	86.29	87.93	35.82	39.35	55.15	82.23	78.91	78.61	73.97
	APER-Adapter	90.91	88.49	77.20	74.02	91.29	91.18	39.92	41.36	55.62	85.14	80.33	80.43	74.66
	SD-LoRA	92.31	88.89	73.82	65.05	76.87	84.29	57.29	39.22	48.28	21.40	35.45	25.52	59.03
	CL-LoRA	92.41	90.87	84.83	80.63	82.82	89.25	59.71	43.77	56.43	84.47	79.66	77.74	76.88
	ENGINE	86.87	87.12	86.21	85.98	86.32	92.97	69.69	68.79	94.03	89.86	85.04	85.09	84.83
	RanPAC	90.93	91.27	77.71	77.32	92.97	98.83	68.10	68.29	67.77	90.05	86.04	86.12	82.95
VILA (Ours)	95.09	94.72	89.81	89.16	93.16	99.35	76.26	75.74	94.19	93.32	89.43	89.53	89.98	

zero-shot reasoning capability of the VLM to rectify potential misclassifications.

Efficient candidate filtering. Directly matching the image against all accumulated class texts is computationally expensive and prone to false positives from irrelevant classes. Instead, we utilize the analytic prediction \hat{y}_{AL} as a high-quality proposal generator. We extract the indices of the top- K logits to form a candidate set $\mathcal{K} = \text{TopK}(\hat{y}_{AL}, K) \subset C_{0:t}$. This ensures that semantic verification is only performed on the most plausible classes, significantly reducing inference latency.

Sparse semantic refinement. For each class $c \in \mathcal{K}$, we construct a robust textual prototype \mathbf{F}_{TXT}^c . To mitigate sensitivity to linguistic phrasing, we employ a prompt ensemble strategy \mathcal{P} , averaging embeddings from diverse templates (see Appendix C) to obtain the final prototype:

$$\mathbf{F}_{TXT}^c = \frac{1}{|\mathcal{P}|} \sum_{p \in \mathcal{P}} f_{CLIP}^{txt}(p(c)) \quad (5)$$

The visual embedding \mathbf{F}_{VIS} is then matched against these specific prototypes. The refinement score vector $\hat{y}_{CLIP} \in \mathbb{R}^{|\mathcal{C}_{0:t}|}$ is computed sparsely:

$$\hat{y}_{CLIP}[c] = \begin{cases} \left\langle \frac{\mathbf{F}_{VIS}}{\|\mathbf{F}_{VIS}\|_2}, \frac{\mathbf{F}_{TXT}^c}{\|\mathbf{F}_{TXT}^c\|_2} \right\rangle & \text{if } c \in \mathcal{K} \\ 0 & \text{otherwise} \end{cases} \quad (6)$$

The final prediction is obtained by fusing the analytic posterior and the semantic prior: $\hat{y} = \hat{y}_{AL} + \hat{y}_{CLIP}$. This ensures an optimal trade-off: the analytic solver handles the bulk of discrimination efficiently, while CLIP provides fine-grained semantic verification for the most ambiguous boundaries.

Algorithm summary. The complete implementation is provided in Appendix B. We explicitly decouple the initial optimization

(gradient descent) from the incremental analytic updates (recursive RLS), ensuring the computational overhead is incurred only once during the entire lifecycle.

5 EXPERIMENTS

Datasets. To verify the robustness of VILA across diverse visual domains and granularity levels, we conduct comprehensive evaluations on 8 benchmarks: (1) *Coarse-grained object recognition*: CIFAR100 [33] and ImageNet-R [34]; (2) *Fine-grained classification*: CUB200 [35] (Birds), FGVC-Aircraft [36], StanfordCars [37], and Food101 [38]; (3) *Scene & action recognition*: UCF101 [39] and SUN397 [40]. We select a subset of classes: 100 classes for CIFAR, Aircraft, Cars, Food, and UCF; 200 classes for ImageNet-R and CUB; 300 classes for SUN. All classes are randomly shuffled.

Implementation details. We construct the specialized branch using a ViT-B/16 [41] backbone equipped with the Adapters, and the universal branch using a frozen CLIP-ViT-B/16 (LAION-400M pre-trained) [42]. The feature dimensions are $D = 768$ and $D_C = 512$, respectively. We train the Adapter on the first task using the AdamW optimizer with an initial learning rate of 0.01, decaying via a cosine annealing schedule. The random buffer dimension is set to $D_B = 16384$. For the regularization hyperparameter λ , we employ a self-adaptive selection strategy. We perform leave-one-out cross-validation (LOOCV) on the base task to automatically select the optimal λ from the candidate set $\{10^{-8}, 10^{-7}, \dots, 10^0\}$. All experiments are implemented in PyTorch and conducted on a single NVIDIA RTX 4090 GPU. We report results over 5 distinct global random seeds: {1993, 1, 56, 254, 602}.

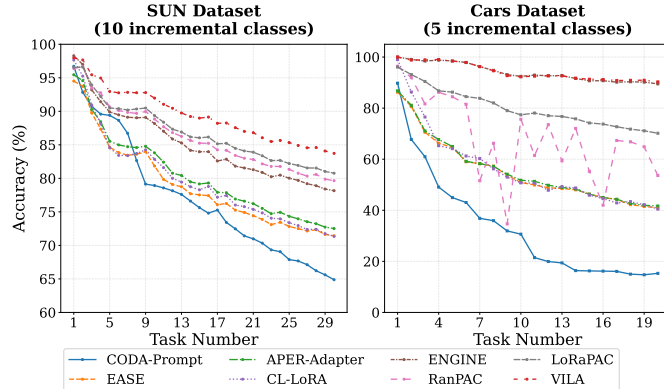


Figure 3: Incremental performance trajectory. Comparison of step-wise accuracy on SUN (Left, $T = 30$) and Cars (Right, $T = 20$). VILA demonstrates superior stability and resistance to forgetting compared to SOTA methods. See *Appendix D* for more figures.

Table 3: Performance comparison under strict online learning setting (1 epoch).

Method	ImageNet-R ($T = 10$)		CUB ($T = 20$)	
	A_T	\bar{A}	A_T	\bar{A}
L2P	64.57 ± 0.46	70.11 ± 0.80	50.13 ± 1.41	65.08 ± 1.36
DualPrompt	61.48 ± 0.35	67.66 ± 0.77	47.94 ± 2.12	61.83 ± 3.21
CODA-Prompt	58.23 ± 0.53	62.96 ± 0.88	30.66 ± 1.32	42.38 ± 2.00
EASE	64.69 ± 0.76	66.90 ± 1.03	84.33 ± 0.41	89.77 ± 0.84
APER-Adapter	65.96 ± 4.81	69.65 ± 1.42	85.22 ± 0.02	90.39 ± 0.81
SD-LoRA	67.27 ± 4.20	70.26 ± 9.08	46.41 ± 2.99	65.29 ± 1.63
CL-LoRA	72.17 ± 0.63	77.52 ± 0.90	80.66 ± 0.87	88.06 ± 0.93
ENGINE	79.53 ± 0.18	85.67 ± 0.66	59.12 ± 0.26	77.12 ± 1.32
RanPAC	71.75 ± 0.30	77.17 ± 0.80	88.92 ± 0.39	92.84 ± 0.80
LoRanPAC	75.23 ± 0.82	79.72 ± 0.94	90.26 ± 0.25	93.53 ± 0.68
VILA	84.52 ± 0.27	88.97 ± 0.45	89.37 ± 0.36	93.23 ± 0.58

Baselines. We benchmark VILA against a comprehensive suite of SOTA methods categorized by their adaptation mechanism: (1) *Prompt-based*: L2P [3], DualPrompt [4], CODA-Prompt [43]; (2) *Adapter-based*: EASE [20], APER-Adapter [21]; (3) *LoRA-based*: SD-LoRA [23], CL-LoRA [24]; (4) *VLM-based*: Engine [28]; (5) *Analytic-based*: RanPAC [11], LoRanPAC [12].

Evaluation Metrics. We report two standard metrics: (1) Average accuracy $\bar{A} = \frac{1}{T} \sum_{t=1}^T Acc_t$: The mean of test accuracies across all incremental stages, where Acc_t is the accuracy on all seen classes $C_{0:t}$ after learning task t . (2) Last-task accuracy A_T : The final accuracy on all classes after the entire sequence is learned, reflecting the ultimate plasticity-stability trade-off.

5.1 Benchmark comparison

Quantitative superiority. Table 2 presents a comprehensive comparison against SOTA PTM-based methods. VILA sets a new standard for analytic learning, outperforming existing approaches by substantial margins of **5.42%** in A_T and **4.75%** in \bar{A} . This stems from three factors: (1) *Fine-grained adaptation*. The specialized branch mitigates representation rigidity to capture subtle inter-class distinctions (e.g., exceeding LoRanPAC by +20.11% on Cars and +6.24% on Aircraft). (2) *OOD robustness*.

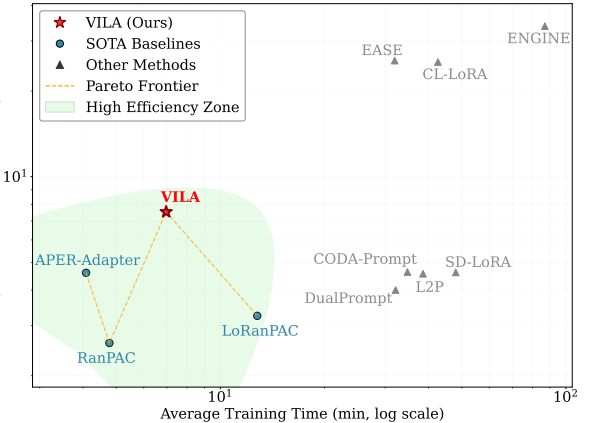


Figure 4: Comparison of total training vs. inference time averaged over 8 datasets ($T = 20$ for all). VILA occupies the high efficiency zone, offering the best trade-off by being significantly faster than complex baselines while outperforming lighter methods.

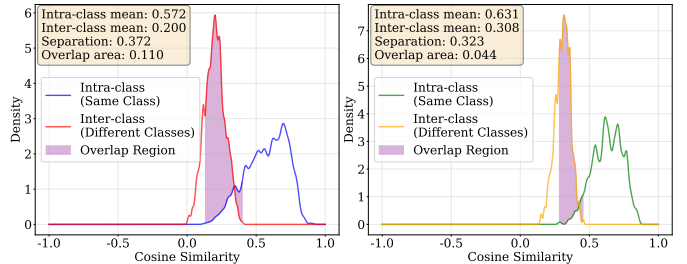


Figure 5: Comparison to the baseline (left) and with UGC (right) on ImageNet-R. We visualize the density estimation of cosine similarities for intra-class (green/blue) and inter-class (orange/red) pairs. The shaded area (colored in purple) quantifies the confusion region.

The geometric calibration aligns heterogeneous subspaces to enable robust generalization under domain shifts (e.g., exceeding ENGINE by +4.17% on ImageNet-R). (3) *Long-term stability*. The frozen universal anchor circumvents parameter drift to prevent catastrophic forgetting in long sequences (e.g., maintaining 89.53% on SUN where others often collapse).

Sequential stability. Figure 3 visualizes the step-wise trajectory. On Cars dataset, VILA maintains a smooth curve, effectively insulating the model from the severe volatility observed in RanPAC. On SUN dataset, it exhibits the slowest decay rate, surpassing the nearest competitor by $\sim 3.0\%$ at the final task. These results confirm that the universal branch serves as a stable semantic anchor, preventing decision boundary drift over long sequences.

One-pass online learning. In the strict 1-epoch setting (Table 3), VILA exhibits minimal degradation and consistently outperforms SOTA baselines (e.g., +4.99% on ImageNet-R). Unlike gradient-based methods that suffer from under-fitting due to insufficient updates, VILA’s recursive analytic solver derives mathematically optimal solutions instantaneously, ensuring superior data efficiency.

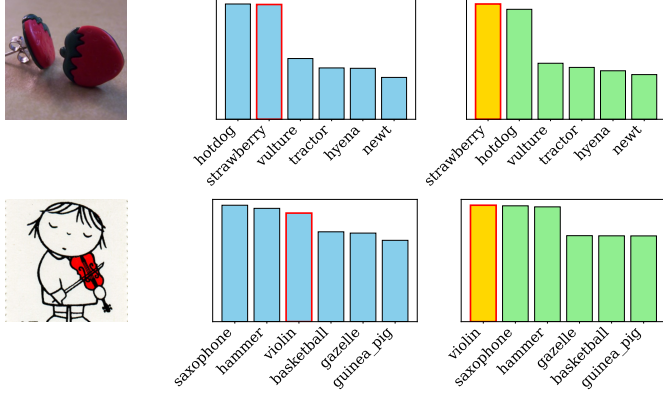


Figure 6: Correction on hard samples on ImageNet-R. Blue bars show baseline misclassifications (w/o CSE). Green/Yellow bars show VILA rectifies these hallucinations via semantic context (w CSE).

Table 4: Component ablation study. DB is dual-branch framework.

DB	UGC	CSE	Aircraft ($T = 10$)		Cars ($T = 10$)	
			A_T	\bar{A}	A_T	\bar{A}
✓			59.12 \pm 0.57	68.99 \pm 1.54	68.27 \pm 1.06	77.70 \pm 1.39
✓	✓		65.28 \pm 0.64	74.83 \pm 1.45	84.13 \pm 1.00	90.43 \pm 0.51
	✓		67.24 \pm 0.35	76.53 \pm 1.37	90.45 \pm 0.36	94.33 \pm 0.70
✓	✓		59.87 \pm 0.52	69.52 \pm 1.43	73.43 \pm 0.76	81.51 \pm 0.89
✓	✓	✓	65.40 \pm 0.51	75.00 \pm 1.46	85.18 \pm 0.95	90.98 \pm 0.58
✓	✓	✓	67.26\pm0.46	76.60\pm1.34	90.58\pm0.40	94.47\pm0.71

Efficiency trade-off. Figure 4 places VILA on the optimal *Pareto frontier*. VILA requires only ~ 7 mins for training and ~ 7.5 mins for inference. This strikes a superior balance between latency and accuracy, avoiding the computational overhead of heavy adapters or iterative optimization common in prior arts (See details per dataset in *Appendix E*).

5.2 Case Study

Geometric calibration (UGC). Figure 5 quantifies discriminability. The baseline suffers from severe intra/inter-class overlap (0.110), causing confusion. VILA aggressively compresses this overlap by $\sim 60\%$ (to 0.044) and shifts intra-class coherence towards 1.0. This confirms UGC acts as a geometric regularizer, effectively sharpening decision boundaries.

Semantic correction (CSE). Figure 6 demonstrates robustness against visual-semantic mismatches. While the baseline misclassifies deceptive samples (e.g., “strawberry earring” \rightarrow “hotdog”) due to texture bias, CSE successfully rectifies these hallucinations. By leveraging universal semantics, VILA suppresses low-level visual noise and enforces semantically consistent predictions.

5.3 Ablation Study

Core component analysis. Table 4 validates each module’s contribution. The dual-branch (DB) architecture forms the critical backbone, yielding the largest gain. Building on this, UGC further boosts performance by aligning heterogeneous subspaces,

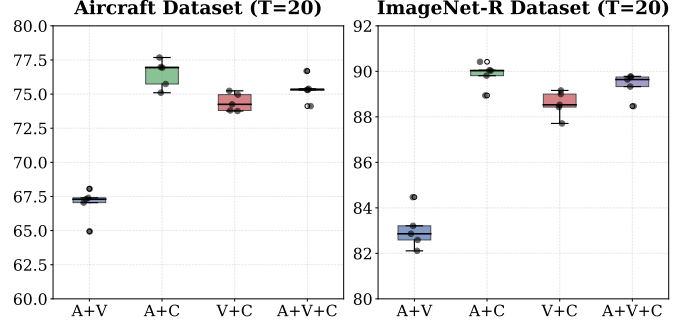


Figure 7: Paradigm integration ablation study (\bar{A}). “V” is frozen ViT, “C” is frozen CLIP, and “A” is ViT-Adapter.

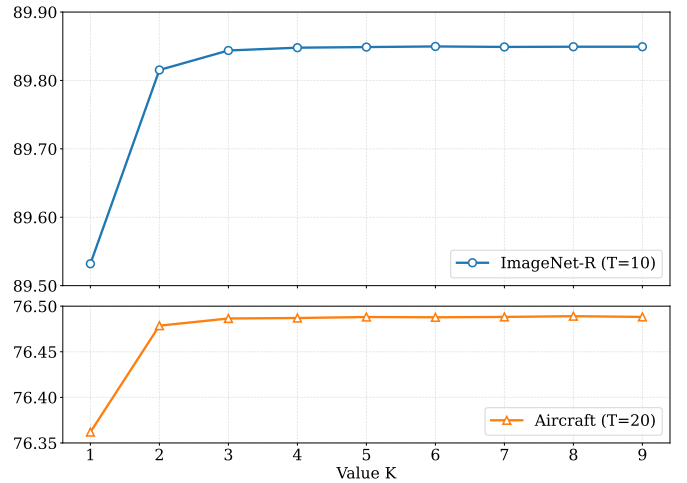


Figure 8: Ablation study (\bar{A}) of the number K .

while CSE provides complementary semantic refinement. Their combination achieves optimal performance, confirming the synergy of geometric constraints and semantic correction.

Paradigm Integration. Figure 7 compares feature sources. The combination of learnable Adapters with frozen CLIP features ($A+C$) consistently outperforms the ViT-based counterpart ($A+V$), highlighting the superiority of CLIP’s open-world priors for CIL. Notably, fusing all features ($A+V+C$) leads to slight drops due to representational redundancy.

Sensitivity to K . Figure 8 shows that performance improves initially and saturates rapidly at $K = 5$, with negligible fluctuations ($< 0.1\%$) thereafter. This demonstrates that VILA extracts sufficient context from a small neighborhood and remains highly robust to hyperparameter variations.

6 CONCLUSION AND DISCUSSION

In this paper, we propose VILA, a dual-branch analytic framework that harmonizes task-specific plasticity with universal semantic stability via a two-level calibration strategy. Extensive experiments demonstrate that VILA establishes a new Pareto frontier in efficiency and accuracy, particularly for fine-grained and long-sequence CIL. Ultimately, this work suggests that analytic learning offers a promising and resource-efficient al-

ternative to gradient-based paradigms for adapting foundation models.

Limitations and Future Work. Despite these advances, three limitations remain for future exploration. *First*, the dual-branch architecture inherently doubles the inference parameter count. Future work could explore knowledge distillation to condense the model for resource-constrained edge deployment. *Second*, the memory consumption of the analytic solver grows quadratically $O(D_B^2)$ with the feature dimension, posing a bottleneck for extremely high-dimensional representations that may require low-rank approximations. *Third*, freezing the specialized backbone after the initial task assumes a consistent domain distribution. While most existing methods also struggle in such heterogeneous settings, this strategy may be suboptimal for drastic mixed-granularity streams. Investigating adaptive mechanisms may better handle these domain shifts.

REFERENCES

- [1] Michael McCloskey and Neal J Cohen. Catastrophic interference in connectionist networks: The sequential learning problem. In *Psychology of learning and motivation*, volume 24, pages 109–165. Elsevier, 1989.
- [2] Marc Masana, Xialei Liu, Bartłomiej Twardowski, Mikel Menta, Andrew D Bagdanov, and Joost Van De Weijer. Class-incremental learning: survey and performance evaluation on image classification. *IEEE Transactions on Pattern Analysis and Machine Intelligence*, 45(5):5513–5533, 2022.
- [3] Zifeng Wang, Zizhao Zhang, Chen-Yu Lee, Han Zhang, Ruoxi Sun, Xiaoqi Ren, Guolong Su, Vincent Perot, Jennifer Dy, and Tomas Pfister. Learning to prompt for continual learning. In *Proceedings of the IEEE/CVF conference on computer vision and pattern recognition*, pages 139–149, 2022.
- [4] Zifeng Wang, Zizhao Zhang, Sayna Ebrahimi, Ruoxi Sun, Han Zhang, Chen-Yu Lee, Xiaoqi Ren, Guolong Su, Vincent Perot, Jennifer Dy, et al. Dualprompt: Complementary prompting for rehearsal-free continual learning. In *European conference on computer vision*, pages 631–648. Springer, 2022.
- [5] Yan-Shuo Liang and Wu-Jun Li. Inflora: Interference-free low-rank adaptation for continual learning. In *Proceedings of the IEEE/CVF Conference on Computer Vision and Pattern Recognition*, pages 23638–23647, 2024.
- [6] Anurag Roy, Riddhiman Moulick, Vinay K Verma, Saptarshi Ghosh, and Abir Das. Convolutional prompting meets language models for continual learning. In *Proceedings of the IEEE/CVF conference on computer vision and pattern recognition*, pages 23616–23626, 2024.
- [7] Lu Yu, Haoyu Han, Zhe Tao, Hantao Yao, and Changsheng Xu. Language guided concept bottleneck models for interpretable continual learning. In *Proceedings of the Computer Vision and Pattern Recognition Conference*, pages 14976–14986, 2025.
- [8] Huiyi Wang, Haodong Lu, Lina Yao, and Dong Gong. Self-expansion of pre-trained models with mixture of adapters for continual learning. In *Proceedings of the Computer Vision and Pattern Recognition Conference*, pages 10087–10098, 2025.
- [9] Ping Guo, Michael R Lyu, and NE Mastorakis. Pseudoinverse learning algorithm for feedforward neural networks. *Advances in neural networks and applications*, 1(321-326), 2001.
- [10] Huiping Zhuang, Zhiping Lin, and Kar-Ann Toh. Correlation projection for analytic learning of a classification network. *Neural Processing Letters*, 53(6):3893–3914, 2021.
- [11] Mark D McDonnell, Dong Gong, Amin Parvaneh, Ehsan Abbasnejad, and Anton Van den Hengel. Rancpac: Random projections and pre-trained models for continual learning. *Advances in Neural Information Processing Systems*, 36:12022–12053, 2023.
- [12] Liangzu Peng, Juan Elenter, Joshua Agterberg, Alejandro Ribeiro, and Rene Vidal. Lorancpac: Low-rank random features and pre-trained models for bridging theory and practice in continual learning. In *The Thirteenth International Conference on Learning Representations*, 2025.
- [13] Zijian Gao, Wangwang Jia, Xingxing Zhang, Dulan Zhou, Kele Xu, Feng Dawei, Yong Dou, Xinjun Mao, and Huaimin Wang. Knowledge memorization and rumination for pre-trained model-based class-incremental learning. In *Proceedings of the Computer Vision and Pattern Recognition Conference*, pages 20523–20533, 2025.
- [14] James Kirkpatrick, Razvan Pascanu, Neil Rabinowitz, Joel Veness, Guillaume Desjardins, Andrei A Rusu, Kieran Milan, John Quan, Tiago Ramalho, Agnieszka Grabska-Barwinska, et al. Overcoming catastrophic forgetting in neural networks. *Proceedings of the national academy of sciences*, 114(13):3521–3526, 2017.
- [15] Zhizhong Li and Derek Hoiem. Learning without forgetting. *IEEE transactions on pattern analysis and machine intelligence*, 40(12):2935–2947, 2017.
- [16] Sylvestre-Alvise Rebuffi, Alexander Kolesnikov, Georg Sperl, and Christoph H Lampert. icarl: Incremental classifier and representation learning. In *Proceedings of the IEEE conference on Computer Vision and Pattern Recognition*, pages 2001–2010, 2017.
- [17] Pietro Buzzega, Matteo Boschini, Angelo Porrello, Davide Abati, and Simone Calderara. Dark experience for general continual learning: a strong, simple baseline. *Advances in neural information processing systems*, 33:15920–15930, 2020.
- [18] Chrisantha Fernando, Dylan Banarse, Charles Blundell, Yori Zwols, David Ha, Andrei A Rusu, Alexander Pritzel, and Daan Wierstra. Pathnet: Evolution channels gradient descent in super neural networks. *arXiv preprint arXiv:1701.08734*, 2017.
- [19] Arun Mallya and Svetlana Lazebnik. Packnet: Adding multiple tasks to a single network by iterative pruning. In *Proceedings of the IEEE conference on Computer Vision and Pattern Recognition*, pages 7765–7773, 2018.
- [20] Da-Wei Zhou, Hai-Long Sun, Han-Jia Ye, and De-Chuan Zhan. Expandable subspace ensemble for pre-trained model-based class-incremental learning. In *Proceedings of the Computer Vision and Pattern Recognition Conference*, pages 10099–10109, 2025.

the IEEE/CVF Conference on Computer Vision and Pattern Recognition, pages 23554–23564, 2024.

[21] Da-Wei Zhou, Zi-Wen Cai, Han-Jia Ye, De-Chuan Zhan, and Ziwei Liu. Revisiting class-incremental learning with pre-trained models: Generalizability and adaptivity are all you need. *International Journal of Computer Vision*, 133(3):1012–1032, 2025.

[22] Edward J Hu, yelong shen, Phillip Wallis, Zeyuan Allen-Zhu, Yuanzhi Li, Shean Wang, Lu Wang, and Weizhu Chen. LoRA: Low-rank adaptation of large language models. In *International Conference on Learning Representations*, 2022.

[23] Yichen Wu, Hongming Piao, Long-Kai Huang, Renzhen Wang, Wanhua Li, Hanspeter Pfister, Deyu Meng, Kede Ma, and Ying Wei. Sd-lora: Scalable decoupled low-rank adaptation for class incremental learning. *arXiv preprint arXiv:2501.13198*, 2025.

[24] Jiangpeng He, Zhihao Duan, and Fengqing Zhu. Cl-lora: Continual low-rank adaptation for rehearsal-free class-incremental learning. In *Proceedings of the Computer Vision and Pattern Recognition Conference*, pages 30534–30544, 2025.

[25] Alec Radford, Jong Wook Kim, Chris Hallacy, Aditya Ramesh, Gabriel Goh, Sandhini Agarwal, Girish Sastry, Amanda Askell, Pamela Mishkin, Jack Clark, et al. Learning transferable visual models from natural language supervision. In *International conference on machine learning*, pages 8748–8763. PMLR, 2021.

[26] Jiazu Yu, Yunzhi Zhuge, Lu Zhang, Ping Hu, Dong Wang, Huchuan Lu, and You He. Boosting continual learning of vision-language models via mixture-of-experts adapters. In *Proceedings of the IEEE/CVF Conference on Computer Vision and Pattern Recognition*, pages 23219–23230, 2024.

[27] Muhammad Anwar Ma’sum, Mahardhika Pratama, Savitha Ramasamy, Lin Liu, Habibullah Habibullah, and Ryszard Kowalczyk. Vision and language synergy for rehearsal free continual learning. In *The Thirteenth International Conference on Learning Representations*, 2025.

[28] Da-Wei Zhou, Kai-Wen Li, Jingyi Ning, Han-Jia Ye, Lijun Zhang, and De-Chuan Zhan. External knowledge injection for clip-based class-incremental learning. In *Proceedings of the IEEE/CVF International Conference on Computer Vision (ICCV)*, pages 3314–3325, October 2025.

[29] Huiping Zhuang, Zhenyu Weng, Hongxin Wei, Renchunzi Xie, Kar-Ann Toh, and Zhiping Lin. Acil: Analytic class-incremental learning with absolute memorization and privacy protection. *Advances in Neural Information Processing Systems*, 35:11602–11614, 2022.

[30] Kevin P Murphy. *Machine learning: a probabilistic perspective*. MIT press, 2012.

[31] Ananya Kumar, Aditi Raghunathan, Robbie Matthew Jones, Tengyu Ma, and Percy Liang. Fine-tuning can distort pretrained features and underperform out-of-distribution. In *International Conference on Learning Representations*, 2022.

[32] Polina Kirichenko, Pavel Izmailov, and Andrew Gordon Wilson. Last layer re-training is sufficient for robustness to spurious correlations. In *The Eleventh International Conference on Learning Representations*, 2023.

[33] Alex Krizhevsky and Geoffrey Hinton. Learning multiple layers of features from tiny images. *Handbook of Systemic Autoimmune Diseases*, 1(4), 2009.

[34] Dan Hendrycks, Steven Basart, Norman Mu, Saurav Kadavath, Frank Wang, Evan Dorundo, Rahul Desai, Tyler Zhu, Samyak Parajuli, Mike Guo, et al. The many faces of robustness: A critical analysis of out-of-distribution generalization. In *Proceedings of the IEEE/CVF international conference on computer vision*, pages 8340–8349, 2021.

[35] Catherine Wah, Steve Branson, Peter Welinder, Pietro Perona, and Serge Belongie. The caltech-ucsd birds-200-2011 dataset. *california institute of technology*, 2011.

[36] Subhransu Maji, Esa Rahtu, Juho Kannala, Matthew Blaschko, and Andrea Vedaldi. Fine-grained visual classification of aircraft. *arXiv preprint arXiv:1306.5151*, 2013.

[37] Jonathan Krause, Michael Stark, Jia Deng, and Li Fei-Fei. 3d object representations for fine-grained categorization. In *Proceedings of the IEEE international conference on computer vision workshops*, pages 554–561, 2013.

[38] Lukas Bossard, Matthieu Guillaumin, and Luc Van Gool. Food-101—mining discriminative components with random forests. In *European conference on computer vision*, pages 446–461. Springer, 2014.

[39] Khurram Soomro, Amir Roshan Zamir, and Mubarak Shah. Ucf101: A dataset of 101 human actions classes from videos in the wild. *arXiv preprint arXiv:1212.0402*, 2012.

[40] Jianxiong Xiao, James Hays, Krista A Ehinger, Aude Oliva, and Antonio Torralba. Sun database: Large-scale scene recognition from abbey to zoo. In *2010 IEEE computer society conference on computer vision and pattern recognition*, pages 3485–3492. IEEE, 2010.

[41] Alexey Dosovitskiy. An image is worth 16x16 words: Transformers for image recognition at scale. *arXiv preprint arXiv:2010.11929*, 2020.

[42] Gabriel Ilharco, Mitchell Wortsman, Ross Wightman, Cade Gordon, Nicholas Carlini, Rohan Taori, Achal Dave, Vaishaal Shankar, Hongseok Namkoong, John Miller, Hanneh Hajishirzi, Ali Farhadi, and Ludwig Schmidt. Openclip, July 2021.

[43] James Seale Smith, Leonid Karlinsky, Vyshnavi Gutta, Paola Cascante-Bonilla, Donghyun Kim, Assaf Arbelle, Rameswar Panda, Rogerio Feris, and Zsolt Kira. Coda-prompt: Continual decomposed attention-based prompting for rehearsal-free continual learning. In *Proceedings of the IEEE/CVF conference on computer vision and pattern recognition*, pages 11909–11919, 2023.

A THEORETICAL PROOF OF REPRESENTATION RIGIDITY

In this section, we provide the derivation for **Proposition 3.1**, justifying why the analytic approximation error is lower-bounded by the distribution shift between the initial task \mathcal{P}_1 and a future task \mathcal{P}_t .

Let $f_\theta : \mathcal{X} \rightarrow \mathbb{R}^D$ be the backbone network. After training on Task 1 (\mathcal{P}_1), the parameters are fixed at θ^* . This frozen extractor defines a feature subspace $\mathcal{S}_1 = \text{range}(\mathbf{F}_1) \subset \mathbb{R}^D$, where \mathbf{F}_1 represents the feature matrix of the training data. The Analytic Classifier (AC) computes weights W via Regularized Least Squares (RLS). As the regularization term $\lambda \rightarrow 0$, the AC solution converges to the orthogonal projection of the target y onto \mathcal{S}_1 .

A.1 Step 1: establishing the lower bound

For a sample x from a future task distribution \mathcal{P}_t , let $y \in \mathcal{Y}_t$ be the ground truth target vector. The prediction of the analytic classifier is $\hat{y} = \mathbf{P}_{\mathcal{S}_1}y$, where $\mathbf{P}_{\mathcal{S}_1}$ is the projection operator onto \mathcal{S}_1 . By the projection theorem, the squared error norm can be decomposed as:

$$\|y - \hat{y}\|^2 = \|y - \mathbf{P}_{\mathcal{S}_1}y\|^2 = \|(\mathbf{I} - \mathbf{P}_{\mathcal{S}_1})y\|^2 \quad (7)$$

Since any other classifier (including regularized versions) in the span of \mathcal{S}_1 cannot achieve a lower error than the orthogonal projection on the training set, the expected error $\mathcal{E}_{\text{task}_t}$ on the new task is strictly lower-bounded by this projection residual (the "bias" term):

$$\mathcal{E}_{\text{task}_t} \geq \mathbb{E}_{x \sim \mathcal{P}_t} \left[\|(\mathbf{I} - \mathbf{P}_{\mathcal{S}_1})y\|^2 \right] \quad (8)$$

A.2 Step 2: linking to distribution distance

During the training on Task 1, maximizing the likelihood is equivalent to aligning the feature subspace \mathcal{S}_1 with the principal components of the Task 1 distribution. Let \mathbf{U}_1 be the basis of \mathcal{S}_1 . Ideally, \mathcal{S}_1 captures the dominant variance of \mathcal{P}_1 .

For the future task t , the target function y depends on the latent semantic features inherent to distribution \mathcal{P}_t . Let \mathcal{S}_t denote the ideal subspace that fully spans the semantics of \mathcal{P}_t . The target y essentially lies within \mathcal{S}_t . The projection residual $\|(\mathbf{I} - \mathbf{P}_{\mathcal{S}_1})y\|^2$ measures how much of the "energy" of y lies outside \mathcal{S}_1 . This is geometrically determined by the *Principal Angles* between subspaces \mathcal{S}_1 and \mathcal{S}_t .

We define the *Grassmann Distance* (a metric for subspace distance) as:

$$\text{Dist}(\mathcal{P}_1, \mathcal{P}_t) \approx d_G(\mathcal{S}_1, \mathcal{S}_t) = \|\sin \Theta\|_F \quad (9)$$

where Θ represents the vector of principal angles between the frozen subspace \mathcal{S}_1 and the target subspace \mathcal{S}_t . If \mathcal{P}_1 and \mathcal{P}_t are similar (small distance), $\mathcal{S}_1 \approx \mathcal{S}_t$, and the projection captures most of y . Conversely, if \mathcal{P}_t represents a distinct domain (large distance, e.g., fine-grained vs. coarse), \mathcal{S}_t creates a large angle with \mathcal{S}_1 . Thus, the residual aligns with the subspace distance:

$$\|(\mathbf{I} - \mathbf{P}_{\mathcal{S}_1})y\|^2 \propto \sin^2(\angle(\mathcal{S}_1, y)) \propto \text{Dist}(\mathcal{P}_1, \mathcal{P}_t) \quad (10)$$

Conclusion. Combining Step 1 and Step 2, we obtain the relationship stated in Proposition 3.1:

$$\mathcal{E}_{\text{task}_t} \geq \|(\mathbf{I} - \mathbf{P}_{\mathcal{S}_1})y\|^2 \propto \text{Dist}(\mathcal{P}_1, \mathcal{P}_t) \quad (11)$$

This confirms that representation rigidity (the inability to rotate \mathcal{S}_1 to match \mathcal{P}_t) imposes a fundamental error floor determined by the geometric divergence between tasks.

B VILA ALGORITHM

As shown in Algorithm 1, the **learning phase** of VILA constructs the model parameters via a hybrid optimization strategy, which integrates gradient-based optimization with analytic recursive updates. *Lines 2-3* is specialized subspace construction. We initialize the specialized branch with a pre-trained ViT and adapters. The model is trained solely on the first task \mathcal{D}_1 via standard SGD. This is the only stage involving backpropagation. Once converged, the specialized backbone is permanently frozen. *Lines 4-10* is recursive analytic update. For the entire task stream $t = 1 \dots T$ (including \mathcal{D}_1), VILA employs an incremental analytic learning protocol. For each batch, it extracts heterogeneous features from both branches and performs Unified Geometric Calibration (UGC). The analytic classifier weights W are then updated recursively using the closed-form RLS solution. This allows the decision boundary to evolve incrementally without storing historical data or resuming gradient training.

As shown in Algorithm 2, the **inference phase** executes coarse-to-fine prediction. During inference, the model weights are fixed. The prediction process follows a dual-step refinement logic. *Lines 1-3* is analytic prediction. The test image is processed to obtain the calibrated feature \mathbf{F} . The analytic classifier outputs the primary logits \hat{y}_{AL} . *Lines 4-8* is semantic rectification. To mitigate the rigidity of the fixed backbone, the Candidate Semantic Enhancement (CSE) module selects the Top- K probable classes and computes semantic similarity scores using CLIP text priors. The final prediction is the fusion of the analytic posterior and the semantic prior.

Algorithm 1 Learning phase of VILA

input Task stream $\mathcal{D}_1, \dots, \mathcal{D}_T$; ViT-Adapter f_{ADPT} ; Frozen CLIP f_{CLIP}^{vis} ; Buffer W^B ; Reg. λ .
output Fintuned ViT-Adapter f_{ADPT} ; Continually learned analytic classifier (W, R) .

- 1: Initialize $W \leftarrow \mathbf{0}$, $R \leftarrow \lambda^{-1}I$.
- 2: Optimize adapter parameters in f_{ADPT} on \mathcal{D}_1 via SGD.
- 3: Freeze f_{ADPT} permanently.
- 4: **for** each task t with dataset \mathcal{D}_t **do**
- 5: **for** batch $(x, y) \in \mathcal{D}_t$ **do**
- 6: $\mathbf{F}_{ADPT} \leftarrow f_{ADPT}(x)$; $\mathbf{F}_{VIS} \leftarrow f_{CLIP}^{vis}(x)$
- 7: $\mathbf{F} \leftarrow \left[\frac{\mathbf{F}_{ADPT}}{\|\mathbf{F}_{ADPT}\|_2}; \frac{\mathbf{F}_{VIS}}{\|\mathbf{F}_{VIS}\|_2} \right]$
- 8: $\mathbf{F}^B \leftarrow \sigma(\mathbf{F}W^B)$
- 9: Update R and W using \mathbf{F}^B, y via RLS (Eq. 2)
- 10: **end for**
- 11: **end for**

Algorithm 2 Inference phase of VILA

input Test image x ; Models $f_{ADPT}, f_{CLIP}; W^B$; Classifier W ; Candidate K .
output Predicted class label \hat{y} .

- 1: Extract calibrated feature \mathbf{F} via UGC (Eq. 4).
- 2: Compute projection $\mathbf{F}^B \leftarrow \sigma(\mathbf{F}W^B)$.
- 3: $\hat{y}_{AL} \leftarrow \mathbf{F}^B W$
- 4: $\mathcal{K} \leftarrow \text{TopK}(\hat{y}_{AL}, K)$ ▷ Select top-K candidate indices
- 5: **for** each class $c \in \mathcal{K}$ **do**
- 6: Construct prototype \mathbf{F}_{TXT}^c via Prompt Ensemble (Eq. 5)
- 7: Compute refinement score \hat{y}_{CLIP} via Eq. 6
- 8: **end for**
- 9: $\hat{y} \leftarrow (\hat{y}_{AL} + \hat{y}_{CLIP})$

C DESIGNED TEMPLATES FOR SEMANTIC PROJECTION

To maximize the generalization capability of the universal branch, we utilize a unified set of prompt templates across all benchmarks (CIFAR-100, ImageNet-R, etc.). We do not tune templates for specific datasets, thereby demonstrating the intrinsic robustness of VILA. Specifically, we employ an ensemble of 19 templates designed to capture diverse visual contexts. Let $\{\}$ denote the class label:

```

"itap of {}.",
"art of {}.",
"i love {}!",
"a origami {}.",
"a photo of {}.",
"a video of {}.",
"a example of {}.",
"a bad photo of {}.",
"a good photo of {}.",
"a large photo of {}.",
"a small photo of {}.",
"a old photo of {}.",
"a clean photo of {}.",
"a dirty photo of {}.",
"a blurry photo of {}.",
"a black and white photo of {}.",
"a low contrast photo of {}.",
"a high contrast photo of {}.",
"{} in a video game."

```

The selection of these specific templates is motivated by three objectives crucial for Class-Incremental Learning:

1. *Robustness against image degradation.* We include templates such as "a blurry photo of...", "a bad photo of...", and "low/high contrast...". These prompts explicitly instruct the text encoder to project class semantics into feature regions

corresponding to corrupted or noisy inputs. This geometric alignment improves matching accuracy when the visual backbone encounters varying data quality or distribution shifts in continuous streams.

2. *Accommodation of domain shifts.* To handle non-photorealistic variations, we incorporate style-specific templates like “*art of...*”, “*an origami...*”, and “*...in a video game.*”. This is particularly vital for benchmarks like ImageNet-R, ensuring that the textual prototype is not a rigid point estimate but encompasses a broader semantic volume covering artistic or abstract renditions.
3. *Scale and viewpoint invariance.* We utilize templates such as “*a large/small photo of...*” and “*itap of...*” (Internet slang for “I took a picture”, implying a casual/realistic viewpoint). These descriptions help regularize the embedding against variations in object scale and camera angles, promoting spatially invariant recognition.

By averaging the features from these diverse prompts, we obtain a **mean textual prototype** that is significantly more stable and representative than any single-prompt embedding, effectively reducing the variance caused by linguistic ambiguity.

D MORE INCREMENTAL PERFORMANCE

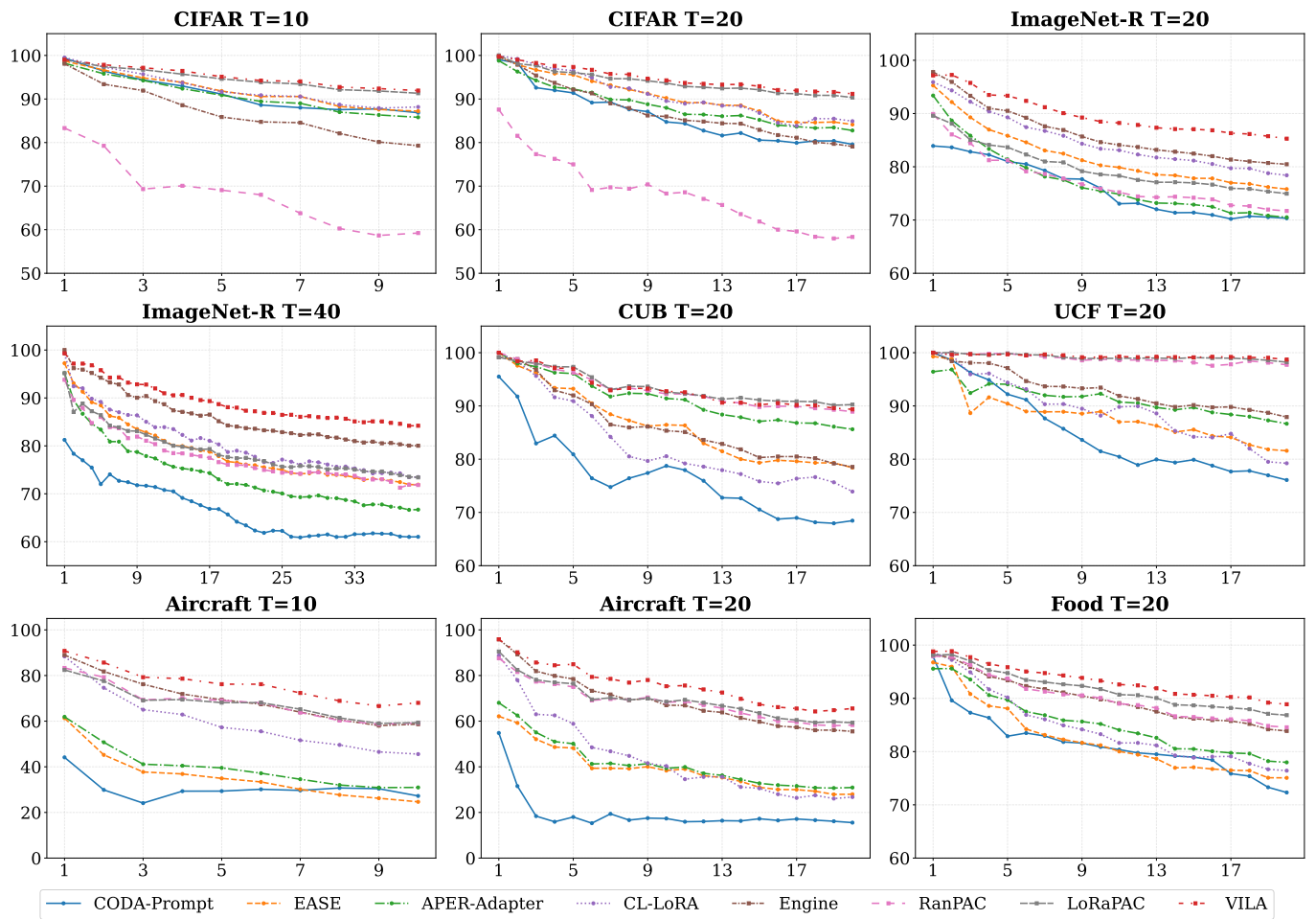


Figure 9: Detailed incremental accuracy curves across different benchmarks. The x-axis represents the number of tasks, and the y-axis denotes the last task accuracy A_T .

To provide a granular view of the learning dynamics, we present the complete incremental accuracy curves across all evaluated settings in Figure 9. These experiments cover diverse scenarios, ranging from standard benchmarks (e.g., CIFAR-100, ImageNet-R) to challenging fine-grained tasks (e.g., CUB-200, FGVC-Aircraft) and varying sequence lengths ($T = 10, 20, 40$).

As observed, our proposed VILA consistently maintains superior accuracy throughout the incremental phases compared to SOTA baselines. Notably, in difficult fine-grained scenarios such as Aircraft $T = 20$ and long-sequence settings like ImageNet-R $T = 40$, where many competitive methods (e.g., RanPAC, CODA-Prompt) exhibit sharp performance degradation, VILA demonstrates remarkable stability and effectively mitigates catastrophic forgetting.

E FULL EFFICIENCY RESULTS

In this section, we provide the details of the computational efficiency for all compared methods across each of the 8 benchmark datasets. While the main text focuses on the average efficiency trade-off, the variability in dataset size (e.g., ImageNet-R vs. CIFAR-100) and complexity (e.g., number of classes) can affect methods differently.

E.1 Training efficiency

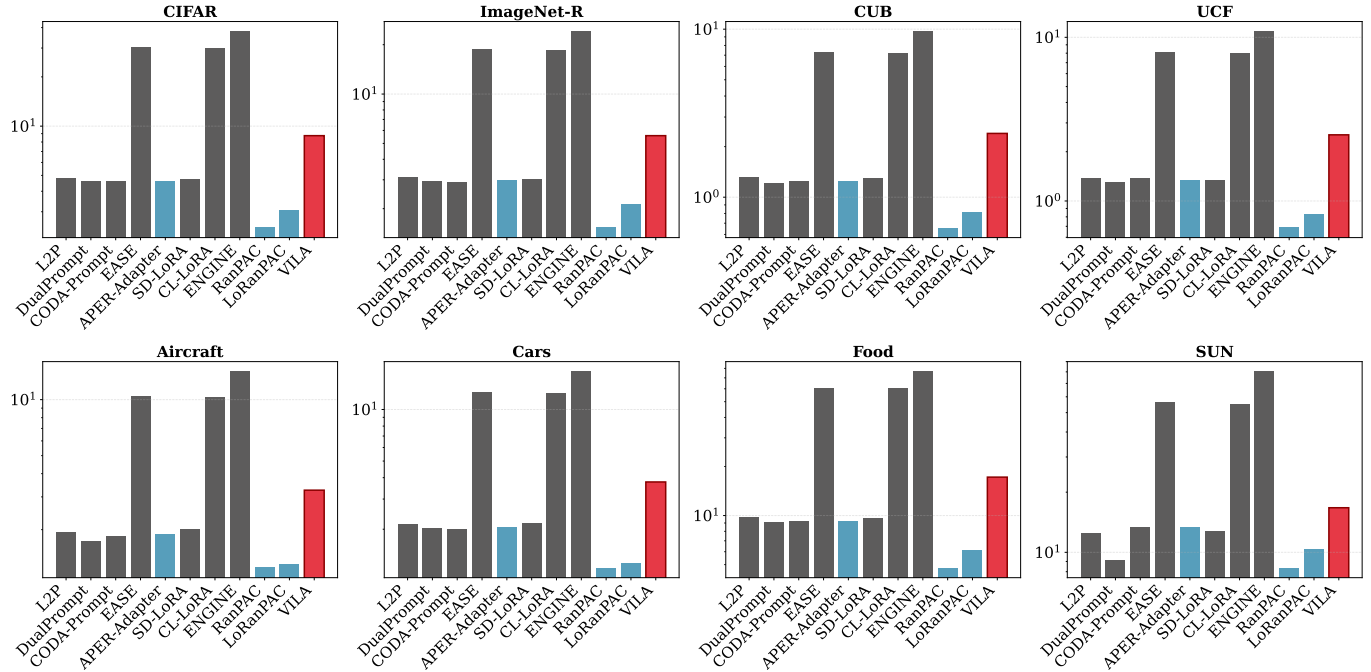


Figure 10: Detailed training time comparison. We report the total training time (in minutes) for all methods across 8 datasets ($T = 20$ for all). The y-axis is plotted on a logarithmic scale to handle the large variance between methods. VILA (red) consistently achieves low training latency, significantly outperforming traditional prompt learning methods (grey) and approaching the speed of the fastest adapters (blue).

Figure 10 illustrates the total training time (in minutes) for each method on individual datasets. Consistent with the average results, VILA (red bars) demonstrates stable and efficient training performance across all scenarios. Notably, on large-scale datasets like *Food* and *SUN*, where heavy optimization-based methods (e.g., ENGINE, EASE) suffer from explosion in training time (exceeding 60 minutes), VILA remains highly efficient (~ 15 minutes), comparable to lightweight adapter-based approaches. This confirms that VILA’s training efficiency is robust to dataset scale and domain shifts.

E.2 Inference efficiency

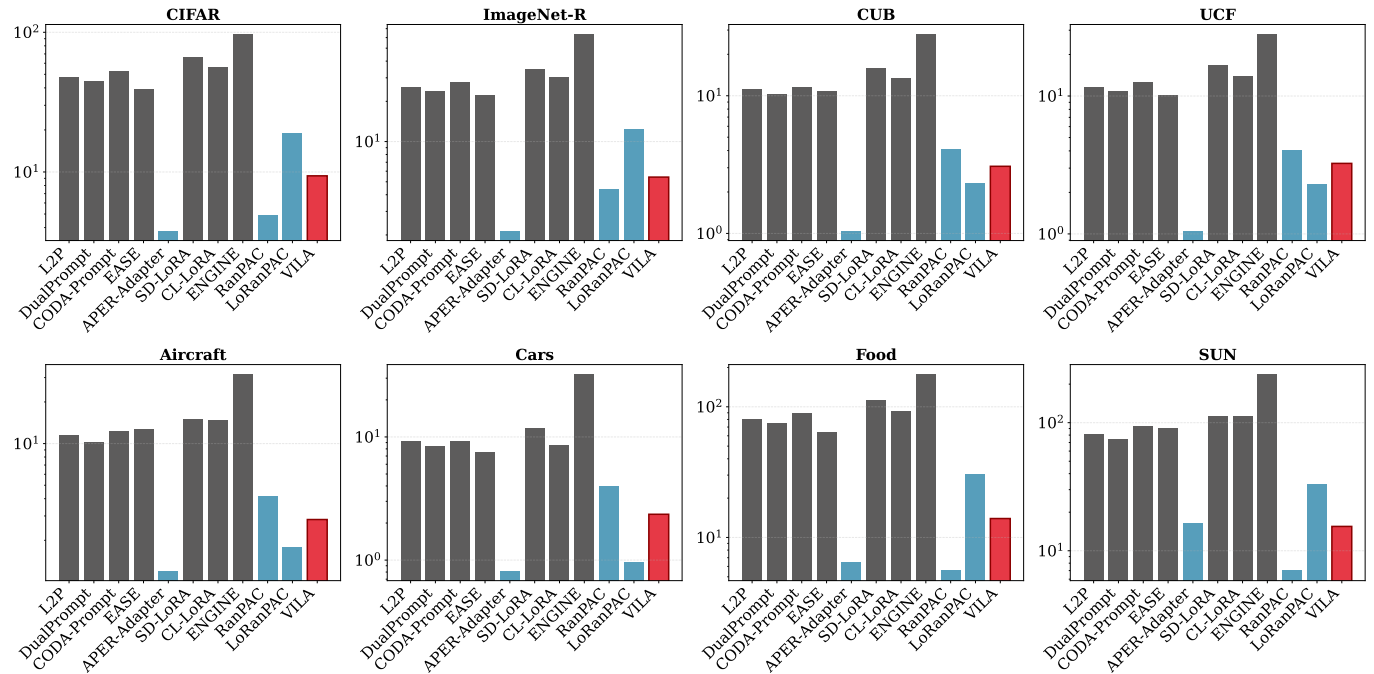


Figure 11: Detailed inference time comparison. We report the total inference time (in minutes) for all methods across 8 datasets ($T = 20$ for all). The y-axis is plotted on a logarithmic scale. VILA (red) maintains competitive inference speeds across all diverse datasets, avoiding the high computational costs associated with heavy baselines like EASE and ENGINE.

Figure 11 presents the total inference time (in minutes) for each dataset. Inference latency is critical for real-world deployment. VILA maintains a low inference overhead, significantly faster than methods involving heavy ensemble or complex attention mechanisms (e.g., EASE, CL-LoRA). Although simple linear probes or ultra-lightweight adapters (e.g., RanPAC) achieve the lowest absolute inference time, VILA strikes a better balance by providing superior accuracy (as discussed in the main text) with only a marginal increase in latency.